

Short-wave infrared continuous-variable quantum key distribution over satellite-to-submarine channels

Qingquan Peng(彭清泉), Qin Liao(廖骎), Hai Zhong(钟海), Junkai Hu(胡峻凯), and Ying Guo(郭迎)
Citation: Chin. Phys. B, 2022, 31 (**6**): 060306. DOI: 10.1088/1674-1056/ac490a
Journal homepage: http://cpb.iphy.ac.cn; http://iopscience.iop.org/cpb

What follows is a list of articles you may be interested in

Parameter estimation of continuous variable quantum key distribution system via artificial neural networks

Hao Luo(罗浩), Yi-Jun Wang(王一军), Wei Ye(叶炜), Hai Zhong(钟海), Yi-Yu Mao(毛宜钰), and Ying Guo(郭迎)
Chin. Phys. B, 2022, 31 (**2**): 020306. DOI: 10.1088/1674-1056/ac2807

Hybrid linear amplifier-involved detection for continuous variable quantum key distribution with thermal states

Yu-Qian He(贺宇千), Yun Mao(毛云), Hai Zhong(钟海), Duang Huang(黄端), Ying Guo(郭迎)
Chin. Phys. B, 2020, 29 (**5**): 050309. DOI: 10.1088/1674-1056/ab8216

Temperature effects on atmospheric continuous-variable quantum key distribution

Shu-Jing Zhang(张淑静), Hong-Xin Ma(马鸿鑫), Xiang Wang(汪翔), Chun Zhou(周淳), Wan-Su Bao(鲍皖苏), Hai-Long Zhang(张海龙)
Chin. Phys. B, 2019, 28 (**8**): 080304. DOI: 10.1088/1674-1056/28/8/080304

Finite-size analysis of continuous-variable quantum key distribution with entanglement in the middle

Ying Guo(郭迎), Yu Su(苏玉), Jian Zhou(周健), Ling Zhang(张玲), Duan Huang(黄端)
Chin. Phys. B, 2019, 28 (**1**): 010305. DOI: 10.1088/1674-1056/28/1/010305

Finite-size analysis of eight-state continuous-variable quantum key distribution with the linear optics cloning machine

Hang Zhang(张航), Yu Mao(毛宇), Duan Huang(黄端), Ying Guo(郭迎), Xiaodong Wu(吴晓东), Ling Zhang(张玲)
Chin. Phys. B, 2018, 27 (**9**): 090307. DOI: 10.1088/1674-1056/27/9/090307

Short-wave infrared continuous-variable quantum key distribution over satellite-to-submarine channels

Qingquan Peng(彭清泉)[1], Qin Liao(廖骏)[2,†], Hai Zhong(钟海)[1], Junkai Hu(胡峻凯)[1], and Ying Guo(郭迎)[1,3,‡]

[1] *School of Automation, Central South University, Changsha* 410083, *China*
[2] *College of Computer Science and Electronic Engineering, Hunan University, Changsha* 410082, *China*
[3] *School of Computer Science, Beijing University of Posts and Telecommunications, Beijing 100876, China*

(Received 18 November 2021; revised manuscript received 31 December 2021; accepted manuscript online 7 January 2022)

The trans-media transmission of quantum pulse is one of means of free-space transmission which can be applied in continuous-variable quantum key distribution (CVQKD) system. In traditional implementations for atmospheric channels, the 1500-to-1600-nm pulse is regarded as an ideal quantum pulse carrier. However, the underwater transmission of this pulses tends to suffer from severe attenuation, which inevitably deteriorates the security of the whole CVQKD system. In this paper, we propose an alternative scheme for implementations of CVQKD over satellite-to-submarine channels. We estimate the parameters of the trans-media channels, involving atmosphere, sea surface and seawater and find that the short-wave infrared performs well in the above channels. The 450-nm pulse is used for generations of quantum signal carriers to accomplish quantum communications through atmosphere, sea surface and seawater channels. Numerical simulations show that the proposed scheme can achieve the transmission distance of 600 km. In addition, we demonstrate that non-Gaussian operations can further lengthen its maximal transmission distance, which contributes to the establishment of practical global quantum networks.

Keywords: continuous-variable quantum key distribution (CVQKD), short-wave infrared, satellite-to-submarine

PACS: 03.67.Dd, 03.67.Hk, 03.67.–a **DOI:** 10.1088/1674-1056/ac490a

1. Introduction

Continuous-variable quantum key distribution (CVQKD) system is one of means of quantum information processing which allows remote participants to share a secret key through an untrusted channel.[1–4] In the traditional CVQKD system, the transmitter Alice encodes the information in the quadrature of the optical field, whereas the receiver Bob decodes the received quantum pulse by using coherence detection. Recently, it has become a hot spot of optical communication technology due to its low cost and high reliability.

With the increasing enhancement of the free-space optical communications, we begin to pay an attention to the security of marine-enabled information for the CVQKD system. Unlike the fiber optic network, the light diffusion effect of quantum pulse transmission in free-space channel is more obvious, and the more interference it receives. Currently, the CVQKD system has been proven to achieve the good performance in free-space channels, such as 500 km in pure atmospheric channel[5] and 50 m in pure seawater channels.[6] However, there is a lack of systematic research in more complex trans-media application scenarios, such as satellite-to-submarine communication. In our previous study, we split the satellite to submarine channel in two through a third party, allowing quantum pulses to be transmitted in two separate channels.[7–9] It is worth noting that the addition of a third party will undoubtedly increase the complexity of the system, which will pose a threat to the stability of the satellite-to-submarine CVQKD scheme. In addition, from the perspective of confidentiality, the existence of a third party is likely to reveal the physical location of the submarine. Therefore, it is necessary for us to study point-to-point satellite-to-submarine quantum communication. There are many difficulties in point-to-point optical communication in free space. For example, due to the light diffusion effect,[10] we must increase the receiving area at destination to obtain the more quantum pulse signals, while ensuring that the receiving area should be made small enough to minimize the transmission of sky-noise photons. The choice of receiving area size is closely tied to the choice of quantum pulse wavelength, making the wavelength the most important and critical part of the practical system.[11–13]

In previous experimental implementations, the 1500-to-1600-nm light is usually regarded as an ideal quantum pulse carrier in the atmospheric channel due to compatibility with current telecom technology, the wavelength-dependent nature of scattering, and lower solar radiance.[14–17] However, the underwater transmission of 1500-to-1600-nm light tends to suffer from severe attenuation, which inevitably deteriorates the security of the satellite-to-submarine system. Therefore, we need to study the parameters of the atmosphere, sea surface, and sea water channel, and establish a complete satellite-

†Corresponding author. E-mail: llqqlq@hnu.edu.cn
‡Corresponding author. E-mail: yingguo@csu.edu.cn

© 2022 Chinese Physical Society and IOP Publishing Ltd

submarine quantum channel model.

To demonstrate the wavelength dependence of satellite-to-submarine quantum communication, we estimate the parameters of the trans-media channels, involving the daytime atmosphere, sea surface and seawater, and find that the short-wave infrared performs well in the above-mentioned channels, which corresponds to the wavelength range of 400–500 nm.[18,19] For more challenging free-space channels, we employ the aggressive spectral filtering techniques (high-order adaptive optics, AO) that allow the use of very tight spatial filtering and relax other filtering requirements.[20,21] In order to evaluate the feasibility of satellite-to-submarine CVKQD, we consider the secret key rate as the performance metric. Through numerical simulation analysis, we find that the satellite can share a string of security keys with submarine with a depth of less than 45 m at an altitude of 60 km. The results will contribute to the development of satellite-to-submarine quantum communication and global quantum networks.

This paper is organized as follows. In Section 2 we suggest the structure of the satellite-to-submarine CVQKD system, which involves the atmospheric, seawater and sea surface channels separately. We demonstrate that shorter wavelengths can be used for satellite-to-submarine quantum communications over trans-media channels. In Section 3 we show the security analysis. Finally, a conclusion is drawn in Section 4.

2. Wavelength optimized CVQKD

The implementation challenges of satellite-to-submarine quantum communications are channel complexity, high optical noise interference and the uncertainty of the environment. The scheme of the satellite-to-submarine-involved CVQKD is shown in Fig. 1, where Alice (satellite) modulates a quantum pulse over a Gaussian state via electro-optical modulators and sends it to Bob (submarine). The quantum pulse has to pass through a turbulent atmosphere, roughness of the sea surface and high-loss seawater before arriving at Bob. Here the atmospheric channel is further divided into a medium Earth orbit (MEO) layer, a low Earth orbit (LEO) layer and a general airspace layer. After receiving the quantum pulse, Bob needs to use adaptive optics to correct the received quantum signals. In what follows, quantum pulses are detected using a local laser generated by a local oscillator (LO) for coherent measurements.[22–24]

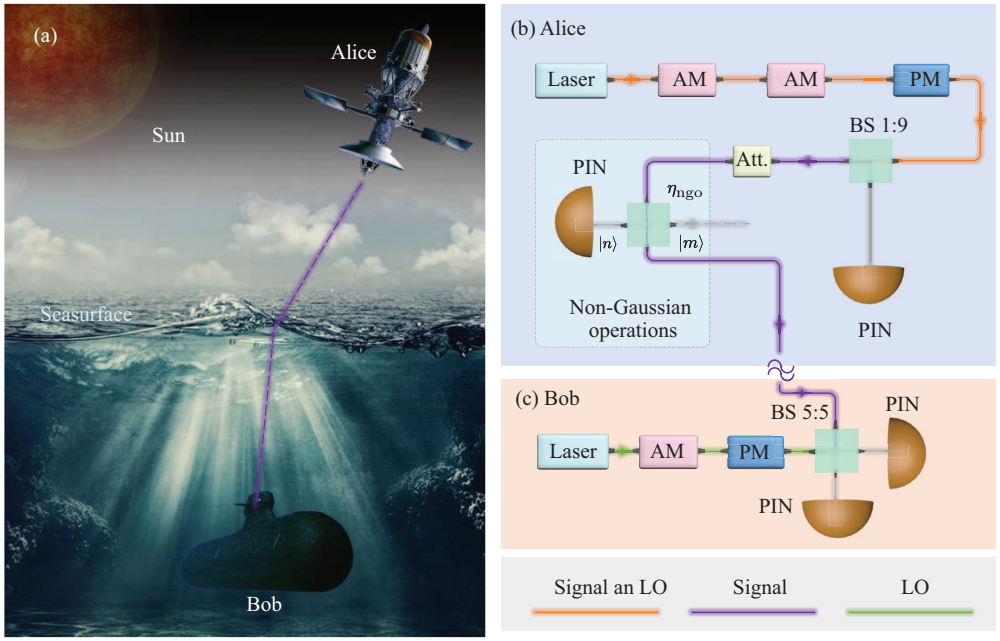


Fig. 1. Short-wave infrared CVQKD over satellite-to-submarine link. (a) Overview of the satellite-to-submarine CVQKD. The link is characterized by actual atmospheric, sea surface and seawater channel. (b) The scheme of short-wave infrared CVQKD over satellite-to-submarine link. The quantum pulses prepared by Alice transmitted through the atmosphere, sea surface and seawater. (c) Bob uses local oscillation for homodyne detection. AM: amplitude modulator; PM: phase modulator; PIN: p–i–n photodiode; η_{ngp}: transmittance of non-Gaussian operations beam splitter; Att.: attenuator; LO: local oscillator; BS: beam splitter.

For the practical implementations, it is necessary to consider the stability and penetration of the quantum pulse itself, as well as the correction of the quantum pulse that can be made using AO technology. We note that the choice of optical wavelength is an indispensable part of laser generation of quantum pulses. In addition, the transmission performance of different light wavelengths is also worth studying.

2.1. Atmospheric turbulence effect

In Fig. 2(a), it illustrates effect of atmospheric turbulence on quantum pulse. The aberrated wavefront results in a narrower diffraction-limited spot (DL spot) than the turbulence-limited spot (TL spot). We note that Bob receives not only quantum pulses, but also sky-noise photons. Therefore, the receiving area of Bob cannot be too small to lose part of

the quantum pulse, nor too large to introduce too many sky-noise photons. In particular, we make use of an AO technique that not only corrects atmospheric turbulence, but also works within the diffraction limit of optical receivers. The AO technique is necessary for performance improvement of the CVQKD system in which narrows spectral filtering will block distorted quantum pulses, and hence enhances the mixing efficiency of homodyne detection. We suggest an LEO satellite downlink structure with the parameters given by $D_{\mathrm{T}} = 10$ cm transmitter, $D_{\mathrm{R}} = 100$ cm receiver, spectral filter efficiency $\eta_{\mathrm{spec}} = 0.9$ and reception efficiency $\eta_{\mathrm{rec}} = 0.5$. The detection efficiency is $\eta_{\mathrm{det}} = 0.8$ for all wavelengths, the initial excess noise is $\varepsilon_0 = 0.01$, and reconciliation efficiency is $\beta = 0.85$.

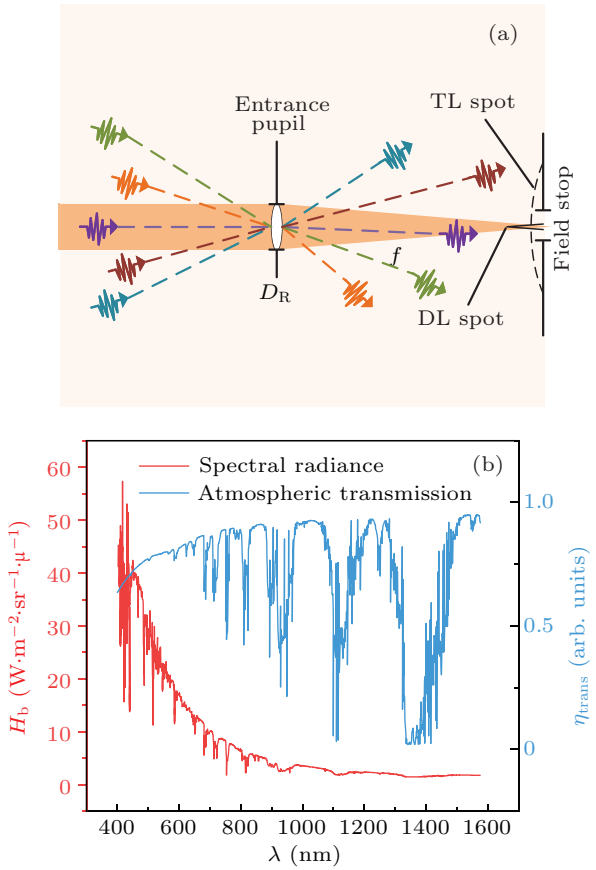


Fig. 2. (a) The filtering process of sky-noise photons in the atmospheric environment and the focusing characteristics in the presence of turbulence are described, where red, orange, blue, green and violet colors correspond to wavelengths of light, respectively. D_{R} is the receiver aperture diameter and f is the receiver focal length. (b) Atmospheric transmission and spectral radiance of receiver pointed to the zenith at 1:00 PM on the winter solstice at 50 km, where the red line represents the spectral radiance H_{b} and the blue line represents the atmospheric transmittance η_{tans}.

In a practical atmospheric environment, we can have ground receiver looking to different points in the sky at different solar positions to obtain different site-dependent downlink scenes for spectral radiance profiles and wavelength dependent transmission. As shown in Fig. 2(b), the atmospheric transmittance and spectral radiance of the zenith receiver at 1:00 PM on the winter solstice with 50 km visibility can be achieved.[25] Considering that wavelength optimization is a key in performance improvement of the satellite-to-submarine communications, the whole spectral structure, in the system design analysis, should include the seawater wavelength range. Although the experimental data demonstrate relatively constant spectral radiance near the wavelength 1550 nm, we choose the wavelength of nearly 400–700 nm for the performance analysis.

The performance of CVQKD is determined by the number of effective quantum pulses received. For a receiver operated at the DL without central obscuration, the field stop can be set to transmit the central peak of the DL Airy pattern to achieve transmitting of 84% of the quantum pulse. The spatial filter diameter is given by

$$D_{\mathrm{spot}}^{\mathrm{DL}} = 2.44\frac{\lambda_{\mathrm{f}}}{D_{\mathrm{R}}}. \tag{1}$$

Then we have the DL solid-angle field of view (FOV)

$$\Omega_{\mathrm{FOV}}^{\mathrm{DL}} = \pi\frac{1.22\lambda}{D_{\mathrm{R}}}^{2}. \tag{2}$$

In the presence of turbulence, we can see a broadened spot size (see the dashed line in Fig. 1), which is caused by the lack of spatial coherence across the entrance pupil resulting in the suppression of the optical receiver's ability to focus received light. Therefore, the TL spot size can be given by[26]

$$D_{\mathrm{spot}}^{\mathrm{TL}} = \frac{D_{\mathrm{spot}}^{\mathrm{DL}}}{\sqrt{S}}, \tag{3}$$

where S is the ratio of the aberrated to the DL-spot peak intensities expressed as

$$S = \left[1 + \frac{D_{\mathrm{R}}}{r(\lambda)}^{5/3}\right]^{-6/5}. \tag{4}$$

The parameter $r(\lambda)$ is the Fried coherence length given by

$$r(\lambda) = r_0\left(\frac{\lambda}{500}\right)^{6/5}, \tag{5}$$

where r_0 is the value measured at 500 nm and λ is the wavelength length in nanometers.[27] It can be considered as a measure of turbulence intensity independent of wavelength, so we choose a spatial filter corresponding to the broadened spot size to obtain the TL solid angle and FOV

$$\Omega_{\mathrm{FOV}}^{\mathrm{TL}} = \pi\left[1.22\frac{\lambda}{D_{\mathrm{R}}}\left(1 + \frac{D_{\mathrm{R}}}{r(\lambda)}^{5/3}\right)^{3/5}\right]^{2}. \tag{6}$$

The loss of spatial filtering can be defined according to the spatial-filtering strategies. The first TL strategy is to always pass 84% of the quantum pulse by increasing the size of the field stop. The second DL strategy does not take the broadened spot size into account and keeps the size of the field stop at the diffraction limit. We take the ratio of the spot-size region to obtain the model

$$\eta_{\mathrm{FS}}^{(\mathrm{TL})} = 0.84,$$

$$\eta_{\mathrm{FS}}^{(\mathrm{DL})} = 0.84 \times S. \tag{7}$$

Subsequently, we have the total atmospheric channel efficiency

$$\eta_{\mathrm{air}}^{(i)}(r_0,\lambda) = \eta_{\mathrm{geo}}(\lambda)\eta_{\mathrm{tran}}(\lambda)\eta_{\mathrm{FS}}^{(i)}(r_0,\lambda)\eta_{\mathrm{spec}}\eta_{\mathrm{rec}}\eta_{\mathrm{det}}, \tag{8}$$

where η_{tran} is the predicted atmospheric transport efficiency, as shown in Fig. 2(b), while i stands in for DL or TL strategy, and η_{geo} is the Gaussian beam equation for geometric aperture-aperture coupling, which can be given by

$$\eta_{\mathrm{geo}} = 1 - \exp\left(-0.5\frac{D_{\mathrm{R}}^2}{w^2(\lambda,z)}\right). \tag{9}$$

Here, the notation $w^2(\lambda,z)$ is the waist function given by

$$w^2(\lambda,z) = w_0^2\left(1+\frac{z^2}{z_{\mathrm{R}}^2(\lambda)}\right), \tag{10}$$

where w_0 is the waist of the signal beam and Z_{R} is the Rayleigh range

$$Z_{\mathrm{R}} = \pi\frac{w_0^2}{2}, \quad w_0 = 0.7\frac{D_{\mathrm{T}}}{2}. \tag{11}$$

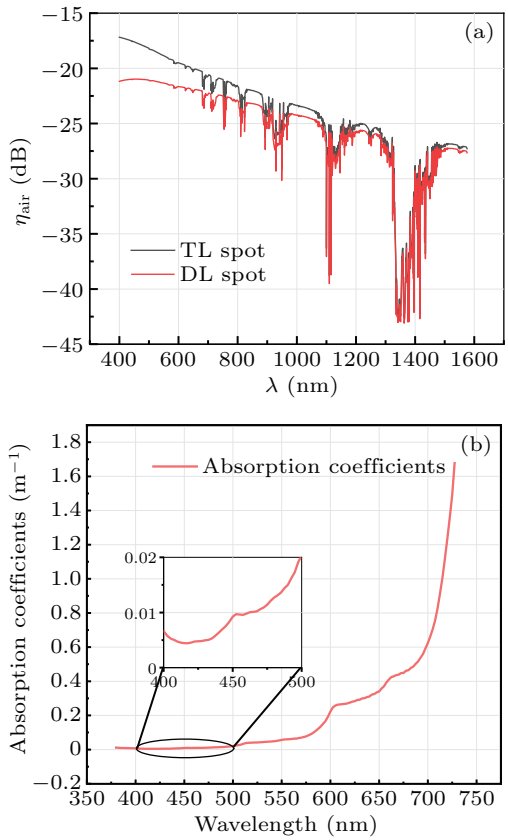


Fig. 3. (a) Total atmospheric channel efficiency corresponding to optical wavelengths. (b) Relationship between light wavelength and absorption coefficient in pure water.[19]

In Fig. 3(a), we show the atmospheric channel efficiency in the optical wavelength range of 400–1600 nm based on the data in Fig. 2(b). The black curve indicates the TL strategy and the red curve indicates the DL strategy. We find that the optical wavelength illustrates a high channel efficiency in the range of 400–700 nm and exhibits a stable upward trend. This result overturns our previous perception that 1550 nm is the best wavelength for atmospheric transmission. It makes possible to establish the practical CVQKD system between satellite and submarine.

2.2. Seawater effect

Similar to the atmospheric channel, the underwater channel is subject to scattering and absorption, as well as attenuation due to beam degradation and drift caused by turbulence. Figure 3(b) shows the effect of the minimum absorption coefficient a_{w} of pure water on the light beam.[19] We find that the absorption coefficient of light from the underwater channel is related to the light wavelength and the minimum absorption coefficient is obtained in the light wavelength range of 400–500 nm.

The seawater can be seen as pure water with impurities, which includes chlorophyll-a concentration, xanthic/humic acid and particles that can affect quantum pulse transmission and bring about signal loss.[28] It can be modeled by depth d, chlorophyll-a concentration to obtain the concentration of particles[29]

$$C_{\mathrm{c}}(d) = \overline{\mathrm{Chla}}_{\mathrm{zeu}}\left(C_{\mathrm{b}} - \frac{sd}{Z_{\mathrm{eu}}} + C_{\mathrm{Max}}\exp\frac{-(d/Z_{\mathrm{eu}}-\zeta_{\mathrm{Max}})^2}{\delta\zeta^2}\right), \tag{12}$$

where Z_{eu} is depth of the euphotic layer, $\overline{\mathrm{Chla}}_{\mathrm{zeu}}$ (mg $\cdot$ m^{-3}) is the column-integrated content of total chlorophyll-a within the euphotic layer, C_{b} is the background chlorophyll-a concentration at the surface, $\delta\zeta$ is the width of the Gaussian peak, C_{max} is the maximum concentration, and the dimensionless depth of the maximum concentration is $\zeta_{\mathrm{Max}} = Z_{\mathrm{Max}}/Z_{\mathrm{eu}}$. The concentrations of humic acid C_{h}, large particles C_{l}, small particles C_{s} and fulvic acid C_{f} can be given by

$$\begin{aligned} C_{\mathrm{h}}(d) &= 0.19334C_{\mathrm{c}}(d)\exp(0.12343C_{\mathrm{c}}(d)),\\ C_{\mathrm{l}}(d) &= 0.76284C_{\mathrm{c}}(d)\exp(0.03092C_{\mathrm{c}}(d)),\\ C_{\mathrm{s}}(d) &= 0.01739C_{\mathrm{c}}(d)\exp(0.11631C_{\mathrm{c}}(d)),\\ C_{\mathrm{f}}(d) &= 1.74098C_{\mathrm{c}}(d)\exp(0.12327C_{\mathrm{c}}(d)). \end{aligned} \tag{13}$$

In addition, scattering spectrum can be calculated versus the wavelength of light, including the scattering spectrum for large particles b_{l}, small particles b_{s}, and pure water b_{w}, as follows:

$$b(\lambda,C_{\mathrm{c}}(d)) = b_{\mathrm{w}}(\lambda) + b_{\mathrm{s}}(\lambda)C_{\mathrm{s}}(d) + b_{\mathrm{l}}(\lambda)C_{\mathrm{l}}(d), \tag{14}$$

where

$$\begin{aligned} b_{\mathrm{l}} &= 0.3411\,(400\,\lambda)^{0.3},\\ b_{\mathrm{s}} &= 0.11513\,(400\,\lambda)^{1.7},\\ b_{\mathrm{w}} &= 0.005826\,(400\,\lambda)^{4.3222}. \end{aligned} \tag{15}$$

Here we have the specific absorption coefficients $a_f = 35.959$ m^2/mg, humic acid $k_f = 0.0189$ nm^{-1}, exponential coefficient for the fulvic acid $a_h = 18828$ m^2/mg, concentration factor of particles $a_c = 0.056$, and chlorophyll $k_h = 0.01105$ nm^{-1}.[30] The absorption spectrum can be similarly given by

$$a(\lambda,d) = a_w(\lambda) + a_f C_f(d)\exp(-k_f\lambda) + a_h C_h(d)\exp(-k_h\lambda) + a_c C_c(d)^{0.602}. \quad (16)$$

Then, the total channel attenuation is given by

$$\alpha(\lambda,d) = a(\lambda,d) + b(\lambda,d), \quad (17)$$

and the light transmittance of seawater is calculated as

$$\eta_{wat} = \exp[-\alpha(\lambda,d)\times d]. \quad (18)$$

In this paper, we consider the beam propagation in the Southern Atlantic Ocean at depth of less than 200 m and temperature of 35 ℃ with the data S4 and S5. Data S4 contains the parameters $\overline{\text{Chla}}_{Zeu} = 0.25$, $\Delta_\zeta = 0.814$, $C_b = 0.57$, $C_{max} = 0.766$, $s = 0.173$, and $Z_{eu} = 80.2$.[29,30] Data S5 contains the parameters $\overline{\text{Chla}}_{Zeu} = 0.388$, $\Delta_\zeta = 0.663$, $C_b = 0.611$, $C_{max} = 0.676$, $s = 0.241$, and $Z_{eu} = 70.3$.[29]

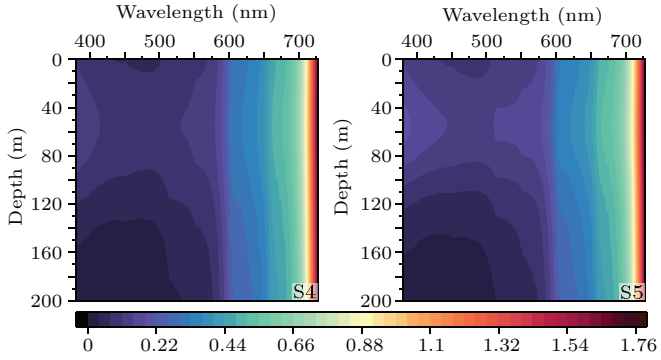


Fig. 4. The resulting attenuation relationships for optical wavelengths and depths.

The attenuation relationships of wavelengths and depths are shown in Fig. 4, where the left figure is the simulation of data S4 and the right figure is the simulation of data S5. Taking the depth into account, we have four layers, i.e., surface layer 0–100 m depth, upper waters ranging 100–120 m depth, intermediate layer 120–160 m, and deep water layer below 160 m, because the surface layer is well mixed with waves, currents and tides. However, as the depth increases, the water temperature decreases, the density increases, and the salinity increases, making it difficult to transmit quantum pulses. The result shows that the attenuation coefficient increases with increasing depth, in which the surface layer performs the best and the deep water layer gets the peak attenuation. From the point of view of light wavelength, we have four regions, i.e., purple region 400–550 nm, blue region 600–650 nm, green region 600–700 nm, red region above 700 nm. The shorter the wavelength, the higher the energy it possesses and the more suitable it is for transmission in seawater. The result shows that as the light wavelength increases, the attenuation coefficient also increases, where the purple region has the best performance, while the red region gets the attenuation peak. Consequently, in the surface layer of seawater, the use of 400–500 nm region wavelengths is more suitable for satellite-to-submarine quantum communications.

2.3. Sea surface effect

The sea surface, which causes refraction and deflection of quantum signals, has an effect on performance of the satellite-to-submarine quantum communications. We consider the effect of the sea surface on the transmitted quantum signals when taking into account zenith angles. The generic wind and wave model is used for our security analysis.[31] It suggests an approach to explain the statistics of the Sun's glitter on the sea surface based on the statistics of slope distribution. We find that the probability distribution of the cross wind slope component is close to a Gaussian distribution, while the probability distribution of the upwind slope component needs to be approximated by some additional higher order moments. Therefore, the Gram–Charlier distribution can be used to represent the statistical characteristics of the sea surface slope. It can be expressed as follows:

$$\begin{aligned} p(Z_u,Z_c) = {} & \frac{1}{2\pi\sigma_u\sigma_c}\exp\left[-\frac{1}{2}\left(Z_u^2+Z_c^2\right)\right] \\ & \times\left[1-\frac{1}{2}c_{21}Z_c(Z_u^2-1)-\frac{1}{6}c_{03}(Z_c^3-3Z_c)\right. \\ & +\frac{1}{4}c_{22}(Z_u^2-1)(Z_c^2-1) \\ & +\frac{1}{24}c_{40}(Z_u^4-6Z_u^2+3) \\ & \left.+\frac{1}{24}c_{04}(Z_c^4-6Z_c^2+3)\right], \end{aligned} \quad (19)$$

where $Z_u = \varepsilon_u/\sigma_u$, $Z_c = \varepsilon_c/\sigma_c$, and the above parameters can be estimated as

$$\begin{aligned} & \sigma_u^2 = 3.16\times10^-3v,\ \ \sigma_c^2 = 0.003+1.92\times10^-3v, \\ & c_{21} = 0.01-0.0086v,\ \ c_{03} = 0.04-0.033v, \\ & c_{22} = 0.12,\ \ c_{40} = 0.4,\ \ c_{04} = 0.23. \end{aligned} \quad (20)$$

Here, the parameter ε_u denotes the upwind with variances σ_u, ε_c corresponds to the upwind with variances σ_c, and v is the wind speed.

In Fig. 5, we show the effect of light propagation on refraction and deflection, which is based on the geometric model of the sea level.[32] We can achieve a circular orbit when taking the height of the satellite into account and the position of the zenith angle. Therefore, the received quantum pulses may be distributed around a circle. The variation of the propagation direction of the quantum pulses across the sea surface is determined by the angle of incidence θ_i and the refractive index of

air and water. Among them, the parameter θ_i can be determined by the local surface slope $\theta_\varepsilon^2 = \varepsilon_u^2 + \varepsilon_c^2$ in the direction $\theta_s = \arctan(\varepsilon_c/\varepsilon_u)$ against the upwind direction and the zenith angle θ_ξ. Then, the refractive index θ_r is calculated according to Snell's law and expressed as $\theta_r = \arcsin(\sin\theta_i n_a/n_w)$, where $n_a = 1.000293$ is the refractive index of air and $n_w = 1.34$ is the refractive index of water.

In Fig. 6, we illustrate the light intensity distribution with changing time propagation direction for the depths of 10, 30 and 50 m. The first column plot indicates that the beam spot at the receiving surface becomes larger as the water depth increases. Compared with the first and second column plots, we find that for the given depth and zenith angle, the higher the wind speed, the larger the receiving surface beam spot becomes. Compared with the plots in the first and third columns, the concentrated distribution of light intensity gradually expands to a ring as the zenith angle increases.

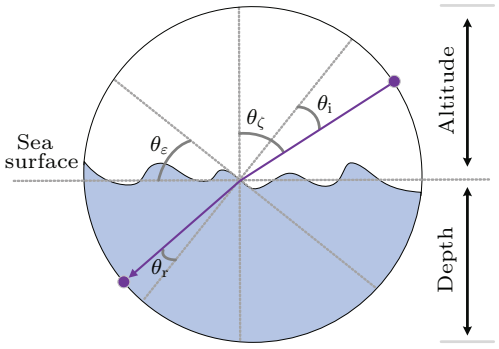


Fig. 5. Geometric model diagram of water surface interference with quantum pulses. The zenith angle of the satellite is represented by θ_ξ; θ_ε corresponds to the slope of the waves, and θ_i and θ_r represent the angle of incidence and refraction of light, respectively.

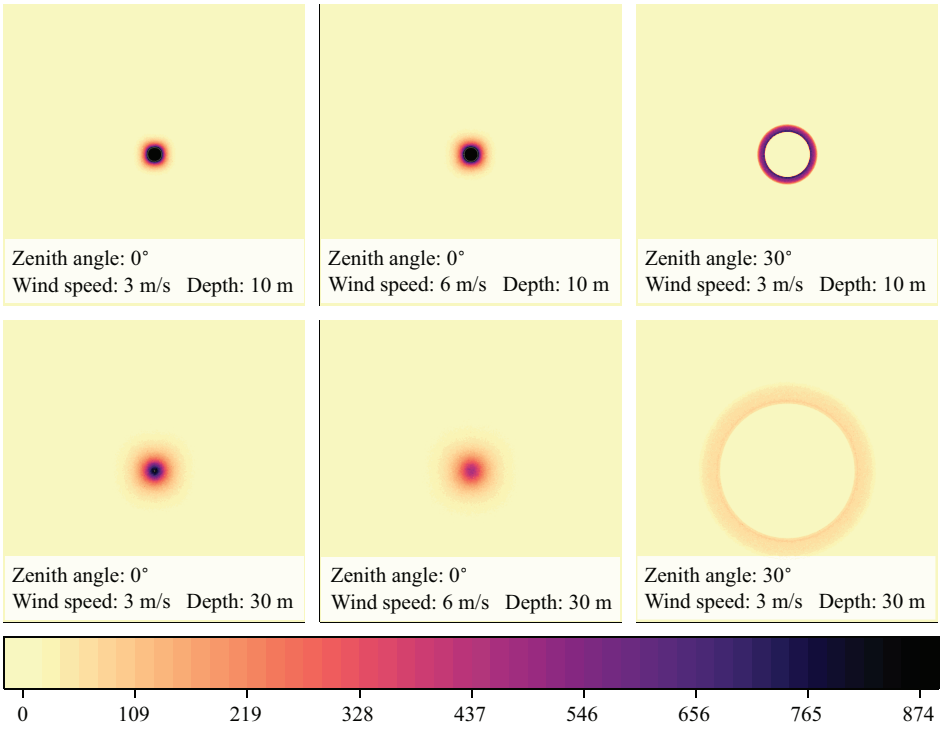


Fig. 6. The light intensity distribution with changing time propagation direction at water depths of 10 m, 30 m and 50 m. The total number of photons for each case in the Monte Carlo simulation is 10^6.

In order to show the effect of the sea surface on the transmittance, it can be obtained by the light deflection efficiency η_{def} and the fraction of transmitted incident light η_{ref}. The parameter η_{def} can be obtained by integrating the received photons.[33] The parameter η_{ref} can be divided into two components, which involves perpendicular

$$\eta_{ref}^{\perp} = 1 - \frac{\sin^2(\theta_i - \theta_r)}{\sin^2(\theta_i + \theta_r)}, \tag{21}$$

and parallel

$$\eta_{ref}^{||} = 1 - \frac{\tan^2(\theta_i - \theta_r)}{\tan^2(\theta_i + \theta_r)}. \tag{22}$$

The total Fresnel[34] transmittance is calculated as

$$\eta_{ref} = 0.5 \times (\eta_{ref}^{\perp} + \eta_{ref}^{||}). \tag{23}$$

Then, the total transmittance of the surface can be derived as $\eta_{sur} = \eta_{def} \times \eta_{ref}$. After that, we have the probability distributions of light transmittance when passing through the sea surface at different wind speeds for zenith angles of 0°, 20° and 30°, as shown in Fig. 7. It is obvious that the transmittance distribution is mainly distributed between 0.97 and 0.99. With the decreasing angle of the zenith angle, the transmittance starts to focus around 0.797. Compared with the zenith angle, the wind speed has little effect on the transmittance distribution.

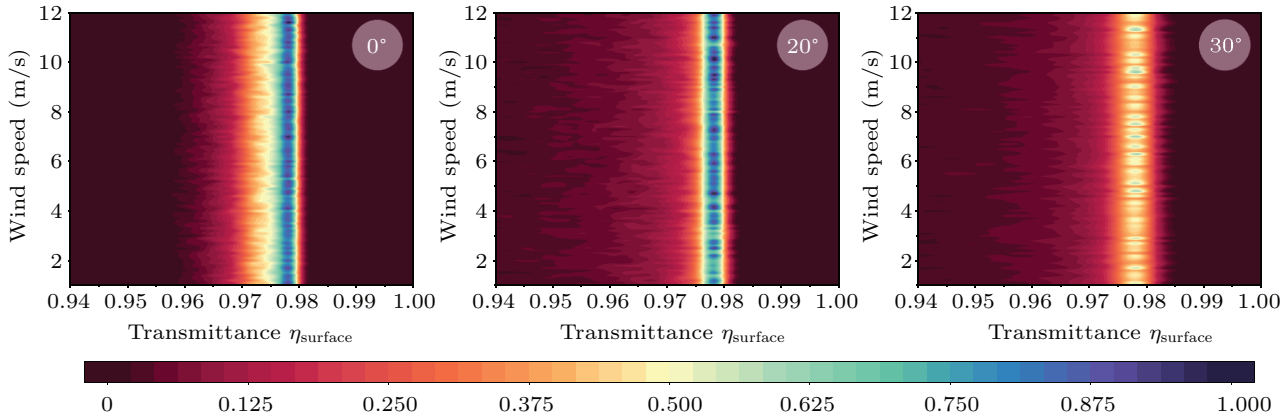


Fig. 7. The light transmittance when passing through the sea surface at different wind speeds for zenith angles of 0°, 20° and 30°. The total number of photons for each case in the Monte Carlo simulation is 10^6.

3. Performance analysis and discussion

3.1. Security analysis

For the security analysis of the satellite-to-submarine CVQKD system, we consider a traditional model of CVQKD with Gaussian modulations, where Alice modulates the initial state with the variance of V_{A}. One half of the state is measured and the other half is transmitted through the atmosphere, sea surface, and seawater in turn, with the total excess noise caused by the background light denoted by χ. Bob measures amplitude or phase quadrature with homodyne detection. We note that the transmittances of the atmosphere, sea surface and seawater fluctuate with time.[35,36]

After being propagated through the fluctuating channel, the overall state degenerates into a non-Gaussian mixed state, so the Wigner function of the overall state is the sum of the Wigner functions of the states weighted by the sub-channel probabilities. Ultimately, the covariance matrix of the mixed state is obtained by means of the transmittance and the mean value of the square root of the transmittance, i.e.,

$$\begin{aligned}\gamma_{\text{AB}} &= \begin{bmatrix} \mathbb{A} & \mathbb{C}\mathbb{Z} \\ \mathbb{C}\mathbb{Z} & \mathbb{B} \end{bmatrix} \\ &= \begin{bmatrix} V\mathbb{I} & \eta_{\text{C}}\sqrt{V^2-1}\mathbb{Z} \\ \eta_{\text{C}}\sqrt{V^2-1}\mathbb{Z} & \eta_{\text{B}}(V-1)+\chi+1 \end{bmatrix}, \end{aligned} \tag{24}$$

with the parameters

$$\begin{aligned} V &= V_{\text{A}}+1, \\ \eta_{\text{B}} &= \langle \eta_{\text{air}} \rangle \langle \eta_{\text{sur}} \rangle \langle \eta_{\text{wat}} \rangle, \\ \eta_{\text{C}} &= \langle \sqrt{\eta_{\text{air}}} \rangle \langle \sqrt{\eta_{\text{sur}}} \rangle \langle \sqrt{\eta_{\text{wat}}} \rangle. \end{aligned} \tag{25}$$

The covariance matrix γ_{AB} shows that the channel effects due to fluctuations can be considered as Gaussian state variance-dependent excess noise.[35]

The secret key rate of satellite-to-submarine CVQKD is derived as

$$K = \beta\left(I_{\text{AB}} - S_{\text{EB}}\right), \tag{26}$$

where β is the reconciliation efficiency, I_{AB} is the mutual information between Alice and Bob, and S_{EB} is the mutual information between Eve and Bob. When both Alice and Bob use homodyne detection, I_{AB} and S_{EB} can be calculated as

$$\begin{aligned} I_{\text{AB}} &= \frac{1}{2}\log_2\left[\frac{\eta_{\text{B}}(\text{V}-1)+\chi+1}{\eta_{\text{B}}(\text{V}+1)+\chi+1-\eta_{\text{C}}^2(\text{V}-1/\text{V})}\right], \\ S_{\text{EB}} &= G\left(\frac{f_1-1}{2}\right)+G\left(\frac{f_2-1}{2}\right) \\ &\quad -G\left(\frac{f_3-1}{2}\right)-G\left(\frac{f_4-1}{2}\right), \end{aligned} \tag{27}$$

with the function $G(x)=(x+1)\log_2(x+1)-x\log_2 x$ and

$$f_{(1,2)} = \frac{1}{2}\left(\Delta \pm \sqrt{\Delta^2-4D^2}\right), \quad f_{(3,4)} = \mathbb{A}\left(\mathbb{A}-\frac{\mathbb{C}^2}{\mathbb{B}^2}\right), \tag{28}$$

where the symbol Δ is given by

$$\Delta = \mathbb{A}^2+\mathbb{B}^2-2\mathbb{C}^2, \quad D = \mathbb{A}\mathbb{B}-\mathbb{C}^2. \tag{29}$$

It shows that Alice's modulation variance V_{A} plays an important role in performance of the system.

In Fig. 8(a), it illustrates the relationship between modulation variance V_{A} and secret key rate. The results show that as the depth of Bob increases, the effect of V_{A} on the secret key rate is weakened and the desirable range is extended. For the given depth, water quality of S4 is more sensitive to V_{A} compared with water quality of S5. In order to obtain the best value of V_{A}, we performed the same simulation experiment in two different water qualities. In the first scenario, Bob is located in the S4 water environment. As shown in Fig. 8(a), the solid lines with red, yellow, and blue represent the underwater transmission distances 10 m, 20 m, and 30 m, respectively. We find that the secret key rate shows a trend of increasing, stabilizing, and decreasing as the V_{A} increases. We also find that the red solid line can obtain the maximum secure key rate around $V_{\text{A}}=2.09$, the yellow solid line can obtain the maximum secure key rate around $V_{\text{A}}=2.01$, and the blue solid line can obtain the maximum secure key rate around $V_{\text{A}}=1.98$. Therefore, we combine the results of the three dashed lines

and consider that the best value range of V_A is 2. In the second scenario, Bob is located in the S5 water quality. Dashed lines in Fig. 8(a) with orange, green, and blue represent the underwater transmission distance is 10 m, 20 m, and 30 m, respectively. Based on the same rule, we believe that the best value range of V_A is 2. Another factor that cannot be neglected in the satellite-to-submarine CVQKD system is the sea surface. If the sea surface conditions are poor, it will result in the transmitted quantum pulse not being well received but being deflected out of the receiving hole, which can be described by using the parameter $\eta_{\rm def}$. In Fig. 8(b), it shows the TL strategy of the secret key rate generation performance. We find that the secret key rate decreases as wind speed increases. Therefore, in order to ensure the proper operation of the satellite-to-submarine CVQKD system, Alice and Bob need to monitor the weather conditions to establish the secret keys.

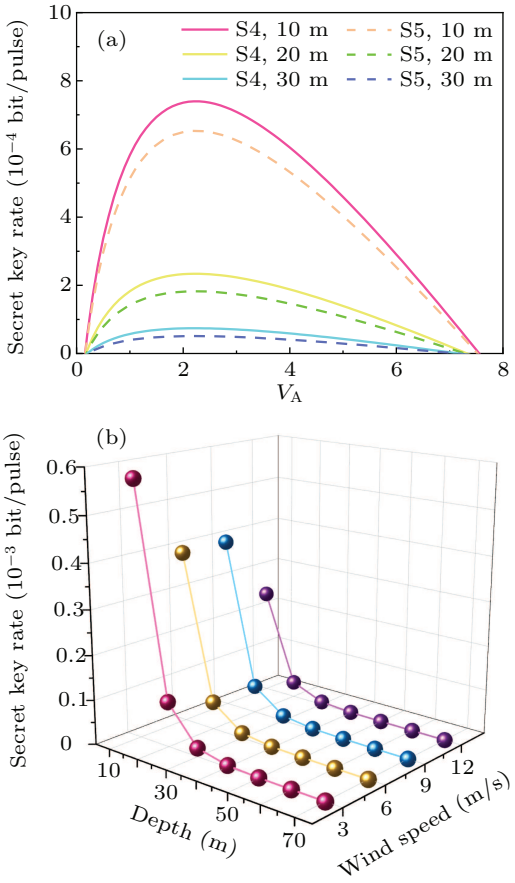


Fig. 8. (a) The secret key rate as a function of different water quality, underwater transmission distance, and modulation variance V_A. Other parameters are set to the winter solstice with high visibility (50 km), the wavelength is 500 nm, and the TL strategy. (b) The secret key rate versus wind speed (3 m/s, 6 m/s, 9 m/s, and 12 m/s) and depths (10 m, 20 m, 30 m, 40 m, 50 m, 60 m and 70 m). The number of photons used for Monte Carlo simulations is 10^6 for each case.

In Section 2, we focus on characteristics in the presence of turbulence in the atmospheric channel and suggest the TD and DL strategies based on two spatial filtering strategies. These two strategies have effect on the secret key rate of the satellite-to-submarine CVQKD system. As shown in Fig. 9, we obtain simulations of the DL strategy and the TL strategy. In both strategies we consider the performance of the system in the flat sea surface case, i.e., wind speed 3 m/s and deflection efficiency $\eta_{\rm def} = 1$. Comparing the TL strategy and the DL strategy, we find that the overall performance of the TL strategy is better than that of the DL strategy, e.g., the TL strategy always obtains a higher secret key rate for the given depth. The simulation results also show that homodyne detection can obtain a higher secret key rate compared with heterodyne detection. It is noteworthy that the secret keys can be successfully established at an altitude of 600 km even in the daytime. In addition, the secret key rate decreases as the depth of Bob increases. The reason is that the transmittance of seawater tends to decrease with increasing depth.

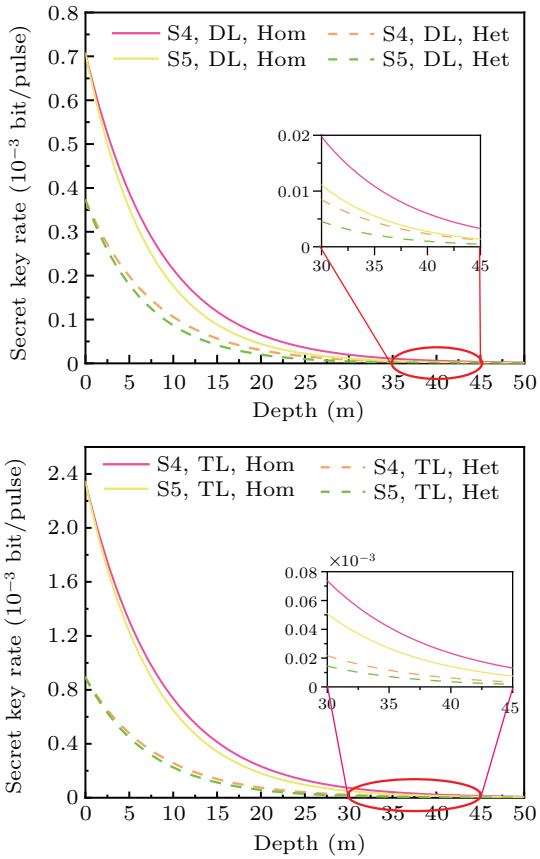


Fig. 9. Simulation diagram of the secret key rate of satellite-to-submarine CVQKD for winter solstice points to the zenith at 1:00 PM and the visibility is 50 km. Het: heterodyne detection; Hom: homodyne detection; wind speed: 3 m/s.

3.2. Photon-catalysis-enabled performance improvement

The security analysis shows that implementing satellite-to-submarine quantum communication with short-wave infrared is feasible. However, the complexity of the free-space channel unavoidably destroys the robustness of quantum pulse, which limits its transmission efficiency. Fortunately, we may enhance quantum pulses with non-Gaussian operations (NGO), such as photon subtraction (PS)[37] photon addition (PA)[38] and quantum catalysis (QC).[39] As shown in

Fig. 1(b), the above operations can be realized with an asymmetrical beam splitter and photon number detector. The case for $m = n$ means the QC operation, while the cases for $m > n$ and $m < n$ are the PA operation and PS operation, respectively. Here, we make use of a QC to regulate potentially deteriorated quantum pulses and thus improve transmission efficiency. In this scheme, the QC-assisted attenuation is a zero-energy-input noiseless attenuation that does not require external energy.[40] So far, the QC operation has been successfully used for improving the performance of the CVQKD system.[39,41] However, there is no implementation of QC in the satellite-to-submarine scene.

We consider the zero-photon catalysis (ZPC), where a vacuum state $|0\rangle\langle 0|$ in auxiliary mode C is injected into the asymmetrical BS with transmittance $\eta_{\rm QC}$ and simultaneously detected at the corresponding output port of BS. It can be expressed as an equivalent operation given by

$$\hat{O} = \mathrm{Tr}\left[\mathrm{BS}(\eta_{\rm QC})|0\rangle\langle 0|\right], \tag{30}$$

where $\mathrm{BS}(\eta_{\rm QC})$ is beam splitter operation with transmittance $\eta_{\rm QC}$. With the help of integration within an ordered product (IWOP) technology,[42] the operation $\mathrm{BS}(\eta_{\rm QC})$ can be expressed as

$$\begin{aligned}\mathrm{BS}(\eta_{\rm QC}) \;=\; &: \exp\left[\left(\sqrt{\eta_{\rm QC}}-1\right)\left(b^{\dagger}b + c^{\dagger}c\right)\right. \\ &\left. + \left(\sqrt{\eta_{\rm QC}}\right)\left(b^{\dagger}c - c^{\dagger}b\right)\right], \end{aligned} \tag{31}$$

where $b^{\dagger}b$ $c^{\dagger}c$ are denoted as the photon operation of input mode and auxiliary mode, respectively. The symbol $: \cdot :$ indicates the normal ordering of operation. Then the mixed state γ_{AB} turns out to be the non-Gaussian state $\gamma_{AB'}$ given by

$$\gamma_{AB'} = \frac{\hat{O}\times\gamma_{AB}}{\sqrt{P_{\rm QC}}}, \tag{32}$$

where $\sqrt{P_{\rm QC}}$ is the success probability of implementing the QC operation that can be calculated as

$$\sqrt{P_{\rm QC}} = \frac{2}{1+(1-\eta_{\rm QC})+\eta_{\rm QC}V}. \tag{33}$$

In Fig. 10(a), we illustrate the secret key rate of the QC-enabled CVQKD system with TL strategy. The results are obtained by performing the optimal $\eta_{\rm QC}$ for the given maximal transmission distance. The numerical simulations show that the QC-assisted attenuation improves the secret key rate compared with the traditional one. In Fig. 10(b), we find that the ZPC performs best for performance improvement of the satellite-to-submarine quantum system in terms of both secret key rate and transmission distance. In addition, the single-photon subtraction performs better than the single-photon addition at the long distance, but the opposite is true at the short distance.

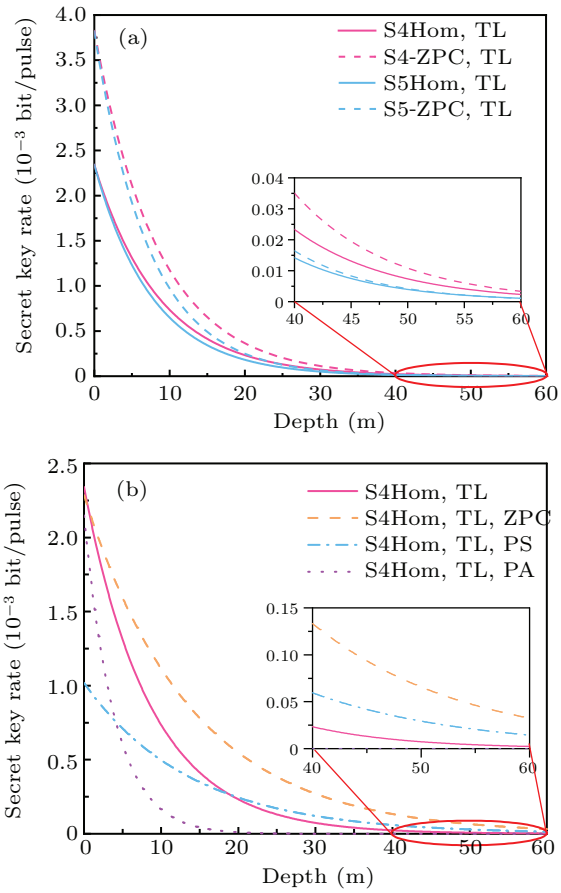


Fig. 10. (a) Simulation diagram of the secret key rate of the QC-enabled satellite-to-submarine CVQKD under TL strategy for winter solstice points to the zenith at 1:00 PM and the visibility is 50 km. (b) Simulation diagram of the secret key rate of the NGO-based satellite-to-submarine CVQKD system with TL strategy. Het: heterodyne detection; Hom: homodyne detection; wind speed: 3 m/s.

4. Conclusion

We have suggested an approach for implementations of the short-wave infrared CVQKD to overcome background-radiation constraints of satellite-to-submarine quantum communications. The atmospheric channel transmittance of the short-wave infrared can be estimated for the quantum pulse which can be transmitted over the satellite-to-submarine channels involving atmospheric, sea surface and seawater. We establish the satellite-to-submarine channel models focusing on atmosphere, sea surface and seawater transmittance. Accounting for these models, we derive the average transmittance in terms of not only zenith angles and wind speed, but also water quality. The results illustrate that it can overcome the satellite-to-submarine channels and achieve effective secret key even for satellite at 600-km orbit and submarine at 60 m depth. In addition, we show effects of non-Gaussian operations on the secret key rate under several strategies, i.e., QC, PA and PS. Most of the parameters are derived from existing experiments, which makes it feasible for the future deployment of a secure global satellite-to-submarine quantum networks.

Acknowledgements

This work was supported by the National Natural Science Foundation of China (Grant Nos. 62101180 and 61871407), the Key R&D Program of Hunan Province (Grant No. 2022GK2016), the State Key Laboratory of High Performance Computing, National University of Defense Technology (Grant No. 202101-25), and the Fundamental Research Funds for the Central Universities (Grant No. 531118010371).

References

[1] Gisin N, Ribordy G, Tittel W and Zbinden H 2002 *Rev. Mod. Phys.* **74** 145
[2] Liao Q, Liu H, Gong Y, Wang Z, Peng Q and Guo Y 2022 *Opt. Express* **30** 3876
[3] Scarani V, Bechmann-Pasquinucci H, Cerf N J, Dušek M, Lütkenhaus N and Peev M 2009 *Rev. Mod. Phys.* **81** 1301
[4] Weedbrook C, Pirandola S, García-Patrón R, Cerf N J, Ralph T C, Shapiro J H and Lloyd S 2012 *Rev. Mod. Phys.* **84** 621
[5] Zuo Z, Wang Y, Liao Q and Guo Y 2021 *Phys. Rev. A* **104** 022615
[6] Xie C L, Guo Y, Wang Y J, Huang D and Zhang L 2018 *Chin. Phys. Lett.* **35** 090302
[7] Guo Y, Peng Q, Liao Q and Wang Y 2021 *IEEE Photon. J.* **13** 1
[8] Liao Q, Liu H, Zhu L and Guo Y 2021 *Phys. Rev. A* **103** 032410
[9] Liao Q, Xiao G, Xu C G, Xu Y and Guo Y 2020 *Phys. Rev. A* **102** 032604
[10] Hughes R J, Nordholt J E, Derkacs D and Peterson C G 2002 *New J. Phys.* **4** 43
[11] Buttler W T, Hughes R J, Lamoreaux S K, Morgan G L, Nordholt J E and Peterson C G 2000 *Phys. Rev. Lett.* **84** 5652
[12] Vasylyev D, Semenov A, Vogel W, Günthner K, Thurn A, Bayraktar Ö and Marquardt C 2017 *Phys. Rev. A* **96** 043856
[13] Gruneisen M T, Eickhoff M L, Newey S C *et al.* 2020 rXiv:2006.07745 [physics.optics]
[14] Heim B, Peuntinger C, Killoran N, Khan I, Wittmann C, Marquardt C and Leuchs G 2014 *New J. Phys.* **16** 113018
[15] Wang S, Huang P, Wang T and Zeng G 2018 *New J. Phys.* **20** 083037
[16] Su Y, Guo Y and Huang D 2019 *Entropy* **21** 908
[17] Liao S K, Yong H L, Liu C, Shentu G L, Li D D, Lin J, Dai H, Zhao S Q, Li B, Guan J Y *et al.* 2017 *Nat. Photon.* **11** 509
[18] Duan Z, Yuan Y, Lu J, Wang J, Li Y, Svanberg S and Zhao G 2020 *Opt. Express* **28** 2600
[19] Pope R M and Fry E S 1997 *Appl. Opt.* **36** 8710
[20] Gruneisen M T, Flanagan M B, Sickmiller B A, Black J P, Stoltenberg K E and Duchane A W 2015 *Opt. Express* **23** 23924
[21] Gruneisen M T, Sickmiller B A, Flanagan M B, Black J P, Stoltenberg K E and Duchane A W 2016 *Opt. Engin.* **55** 026104
[22] Huang D, Huang P, Lin D, Wang C and Zeng G 2015 *Opt. Lett.* **40** 3695
[23] Qi B, Lougovski P, Pooser R, Grice W and Bobrek M 2015 *Phys. Rev. X* **5** 041009
[24] Liao Q, Xiao G, Zhong H and Guo Y 2020 *New J. Phys.* **22** 083086
[25] Lanning R N, Harris M A, Oesch D W, Oliker M D and Gruneisen M T 2021 arXiv:2104.10276 [quant-ph]
[26] Farrell T C 2019 *The effect of atmospheric optical turbulence on laser communications systems: part 1, theory sensors and systems for space applications XII* (International Society for Optics and Photonics) vol 11017 p. 110170B
[27] Roggemann M, Welsh B and Hunt B 1996 *Imaging Through Turbulence* (New York: CRC Press)
[28] Johnson L J, Green R J and Leeson M S 2013 *Appl. Opt.* **52** 7867
[29] Uitz J, Claustre H, Morel A and Hooker S B 2006 *J. Geophys. Res.: Oceans* **111** C08005
[30] Gariano J and Djordjevic I B 2019 *Opt. Express* **27** 3055
[31] Cox C and Munk W 1954 *J. Opt. Soc. Am.* **44** 838
[32] Ross V, Dion D and Potvin G 2005 *J. Opt. Soc. Am. A* **22** 2442
[33] Guo Y, Xie C, Huang P, Li J, Zhang L, Huang D and Zeng G 2018 *Phys. Rev. A* **97** 052326
[34] Hieronymi M 2016 *Opt. Express* **24** A1045
[35] Dong R, Lassen M, Heersink J, Marquardt C, Filip R, Leuchs G and Andersen U L 2010 *Phys. Rev. A* **82** 012312
[36] Guo Y, Xie C, Liao Q, Zhao W, Zeng G and Huang D 2017 *Phys. Rev. A* **96** 022320
[37] Liao Q, Guo Y, Huang D, Huang P and Zeng G 2018 *New J. Phys.* **20** 023015
[38] Hu L, Al-amri M, Liao Z and Zubairy M 2020 *Phys. Rev. A* **102** 012608
[39] Guo Y, Ye W, Zhong H and Liao Q 2019 *Phys. Rev. A* **99** 032327
[40] Zhang Y, Melko R G and Kim E A 2018 *Phys. Rev. B* **97** 079904
[41] Zuo Z, Wang Y, Mao Y, Ye W, Hu L, Huang D and Guo Y 2020 *J. Phys. B: At. Mol. Opt. Phys.* **53** 185501
[42] Fan H Y 1990 *J. Phys. A: Math. Gen.* **23** 1833